Carbon nitride with grafted molecular as electron acceptor and active site to achieve efficient photo-activated peroxymonosulfate for organic pollutants removal

Ling Li [a,b], Hao Zeng [a], Rongdi Tang [a,c], Zhanpeng Zhou [a,b], Sheng Xiong [a], Wenbo Li [a,b], Ying Huang [b,*], Yaocheng Deng [a,*]

[a] *College of Environment & Ecology, Hunan Agricultural University, Changsha 410128, China*
[b] *College of Resources, Hunan Agricultural University, Changsha 410128, China*
[c] *College of Environmental Science and Engineering, Hunan University and Key Laboratory of Environmental Biology and Pollution Control (Hunan University), Ministry of Education, Changsha 410082, China*

ARTICLE INFO

ABSTRACT

The effective activation of peroxymonosulfate (PMS) by polymer carbon nitride (PCN) is hampered by the unpredictable movement and rapid recombination of photocarriers. In this study, niacin served as a beneficial modifier to help constructed the directional electron transfer pathway from the center to the edge in the synthesized PCN catalyst (UCNNA) for efficient PMS activation. The UCNNA/PMS/vis shows the highest kinetic constants (0.050 min^{-1}), which is 2.9-fold increase over the PCN/PMS/vis. The experiments and theoretical calculations indicated that niacin as electron acceptor group prevents the recombination of photocarriers in-plane. Simultaneously, niacin can serve as PMS adsorption site, further facilitating electron transfer and the $^1O_2$ generation. Mass spectrometry analysis and Fukui index calculations confirm the priority of lateral chain oxidation ($^1O_2$ attack site) during atrazine degradation. These results provide new insights into rational design of metal-free catalysts/PMS/vis system, as well as providing guidance and theoretical support for atrazine degradation mechanisms.

1. Introduction

As a highly effective herbicide for weeds, atrazine (ATZ) has been widely used and has provided numerous benefits to crop production over the past decades [1]. Due to only partial absorption by soil and weeds, excess ATZ is continuously released and accumulates in the natural water environment [2]. Currently, ATZ has been detected in various water environments, including seawater, lakes, rivers, and even groundwater [3,4]. Additionally, ATZ has been listed as an endocrine-disrupting chemical that may have harmful effects on human health [5,6]. Hence, it is urgent to find methods to remove ATZ from the contaminated environment. Until now, visible-light-driven photocatalysis, possessing potential for solar energy conversion and degradation of contaminants, is regarded as a promising environmentally friendly technology [7,8]. During the process of photocatalysis, photogenerated electrons, holes, and reactive oxygen species (ROS) effectively facilitate the decomposition of organic compounds by cleaving chemical bonds [9–11]. While photocatalysis has shown promise in degradation pollutants, the recombination of photogenerated electrons and holes have limited its application. High recombination rates can reduce the efficiency of pollutant degradation, especially for persistent and refractory pollutants such as ATZ [12]. Therefore, coupling photocatalysis with other technologies to enhance oxidation efficiency could be another way out for their practical application. So far, piezo-photocatalytic, photo-thermal technology, and photocatalytic coupled biological treatment have been developed and investigated for pollutant degradation [13–16]. Compared to other coupling technologies, the photocatalytic coupled PMS process is considered environmentally friendly, as it harnesses the power of reactive oxygen species to break down pollutants without the need for excessive chemicals or harsh conditions. Additionally, photocatalysts can efficiently introduce energy to activate PMS. Simultaneously, PMS captures electrons, thereby preventing the recombination of photogenerated electrons and holes within the photocatalyst [17,18]. Therefore, the photocatalysis-activated PMS

process has attracted the interest of researchers.

Among many semiconductor photocatalysts, polymer carbon nitride (PCN) shows high chemical stability, facile synthesis, and ease of large-scale production, which makes it popular for achieving environmental pollution remediation [19,20]. However, the effective activation of PMS by PCN is significantly hampered by the unpredictable movement and quick recombination of photogenerated charge pairs. Therefore, researchers have developed various strategies to facilitate the carrier separation of PCN. For example, the loading of metals or metal oxides with PMS activation ability onto PCN, or coupling PCN with other catalysts to accelerate activate PMS can be considered [21,22]. Our previous studies have successfully constructed heterojunction (homojunction) carbon nitride and atomically doped carbon nitride for photocatalytic activation of PMS [23,24]. Although the carbon nitride heterojunction/homojunction hindered the partial carrier recombination, the transfer of charge in the PCN plane is still anisotropic. Some research indicates that the edge functionalization via electron donor or electron acceptor can promote the in-plane carrier separation of PCN by forming different charge densities [25,26]. Therefore, it is believed that an electron acceptor grafted at the edge of PCN with a strong affinity to PMS would greatly improve the PMS photo-activation for efficiently degrade organic pollutants by acting as a reaction center as well as an electron aggregation point. Inspired by these studies, in this work, nicotinic acid (NA) was chosen as an electron acceptor to synthesize NA grafted PCN (UCNNA) with electron directed transfer function. As a small molecule organic acid, NA with a carboxyl group and pyridine ring, is a good candidate for electron acceptor. Moreover, the carboxyl group in NA can react with the amino group in urea to form an amide bond, which is conducive to retaining the PCN structure and reducing the production of adverse defects [27].

In most photocatalysis-activated PMS studies, hydroxyl radical ($\cdot$OH) and sulfate radical ($\bullet SO_4^-$) have been considered as the predominant reactive oxygen species in radical oxidation pathways, because of their high oxidation potential ($E^0_{\bullet OH} = 1.8 \sim 2.7$ V, $E^0_{\bullet SO_4^-} = 2.5 \sim 3.1$ V) [28,29]. Therefore, the high efficiency of pollutant degradation is easily achieved in de-ionized water. However,$\cdot$OH and $\bullet SO_4^-$ in actual wastewater would inevitably be devoured by the coexisting inorganic ions or natural organic matters, thus adversely affecting the treatment performance [20,30]. Compared with radical-based oxidation pathways, non-radical oxidation pathways mediated by electron transfer and non-radical species exhibit distinct selective oxidation of pollutant removal under complex water matrices [31]. Besides, because of their great selectivity toward electron-rich substances and superior resistance to water interference, non-radical oxidation pathways have gained increased attention. Therefore, an increasing number of non-radical oxidation pathways dominated photocatalysis-activated PMS systems have been specially constructed and reported. In previous studies, researchers have paid a lot of attention to investigate the non-radical oxidation pathways dominated photocatalysis-activated PMS systems. For example, Cui et al. demonstrated that the PMS can be activated via electron transfer pathway to achieve efficient generation of $^1O_2$ with effect of boron-doping and surface-defect on g-C$_3$N$_4$ [18]. Weng et al. obtained PCN with high selectivity for $^1O_2$ generation by covalent modification of g-C$_3$N$_4$ [26]. However, most of them focused on removal efficiency and degradation kinetics, but few illustrated the design of PMS adsorption sites and electron aggregation point. Additionally, the origin of $^1O_2$ in photocatalysis-activated PMS systems remains ambiguous. Meanwhile, less research on electron transfer in photocatalysis-activated PMS systems has been carried out, leading to the electron transfer mechanism of photocatalysis-activated PMS systems is still unclear. Hence, exploring the evolution of non-radical pathways provides insights into how non-radical species affect systems in-depth.

Herein, NA was grafted on PCN (UCNNA) to form a stable and highly efficient catalyst for the degradation of ATZ by PMS photo-activation.

The oxidation performance and effect of reaction parameters of the UCNNA/PMS/vis system were investigated. Importantly, by integrating quenching experiments, electron spin resonance (ESR) measurements, electron chemical analyses, and density functional theory (DFT) calculation, the non-radical oxidation species, electron transfer pathways, and active sites were revealed. Furthermore, the attack sites of $^1O_2$ and possible degradation pathways were proposed by the DFT calculation and liquid chromatography-mass spectrometry (LC-MS). The toxicity of ATZ degradation intermediates was assessed by toxicity assessment software and soybean culture experiments. This research unveils the mechanism of the PMS adsorption in catalysts surface and electron transfer, providing a reference for the study of PCN photocatalysts to effectively activate PMS.

2. Materials and methods

2.1. Chemicals and Reagents

The chemical list is provided in Text S1.

2.2. Synthesis of catalyst

To synthesize the polymeric carbon nitride (PCN), 5 g urea in a 30 mL covered ceramic crucible was heated to 500 °C for 2 h in the muffle furnace under an air atmosphere (5 °C/min heating rate).

The NA decorated polymeric carbon nitride sample was prepared as follow. 5 g urea mixed with a certain amount of NA was ground uniformly, and then heated to 500 °C as the above synthetic process of PCN. Based on the amount of NA (20 mg, 40 mg, 60 mg, 80 mg), the resultant samples were labeled as UCNNAX (X = 20, 40, 60, 80).

2.3. Experimental procedures

The degradation of ATZ was performed in a 50 mL flask, with a 30 cm distance between the flask and lamp (a 300 W Xe lamp equipped with a 420 nm UV cut-off filter to simulate the visible light). The typical process was followed, according to which the catalyst was 0.4 g/L, and the initial concentration in the system was 0.2 g/L with the addition of a certain amount of PMS stock solution. The testing experiments were divided into two parts: (1) the catalyst was dispersed into ATZ solution with a 10 s ultrasonic treatment, and then agitated in dark condition for 20 min to establish an adsorption phase equilibrium; (2) with the addition of PMS, the reaction occurred in the following 60 mins illumination. Every 20 min, 1 mL-2 mL of the reaction solution was taken out and filtered using 0.45 μm disposable filters. Unless otherwise stated, all the experiments were conducted at the initial pH without adjustment. All experiments were repeated at least three times.

2.4. Analytical methods

High performance liquid chromatography (HPLC) (Agilent Technologies, USA) on a C18 column was used to determine the residual concentration of ATZ in solution. The mobile phase was a combination of 30% deionized water and 70% methanol, with a flow rate of 0.1 mL·min^{-1} and a detection wavelength was 225 nm. LC-MS was used to identify the ATZ degradation products (The detailed LC-MS measurement condition and the sample preparation are provided in Text S2) [32]. To identification of the electron-transfer process during the UCNNA/PMS/vis system, electrochemical measurements were measured by a CHI 660D workstation. The counter electrode was the Pt electrode, and the reference electrode was the Ag/AgCl electrode. The following is how the functional electrodes were made: 15 mg UCNNA was dispersed into naphthol-ethyl alcohol solution (naphthol:ethyl alcohol=1:1) with 20 min ultrasonic treatment. Then 100 μL mixture was dropped on an FTO glass and dried. Toxicity Estimation Software Tool (T.E.S.T) program (T.E.S.T V 5.1.1) was used to assess the toxicities

of ATZ degradation intermediates using the Bioconcentration factor, development toxicity value, acute toxicity of Daphnia magna LC_{50} (48 h), Oral rat LD_{50}, and Fathead minnow LC_{50} (96 h).

2.5. Theoretical calculation

Detailed DFT calculations in this study can be found in Text S3 of the Supporting Information.

3. Results and discussion

3.1. Characteristics of the catalysts

The possible polymerization reaction is proposed in Fig. 1(a). NA as a precursor to the design of UCNNA was prepared by copolymerization with urea. The urea undergoes a multi-step condensation reaction to form triazine ring unit under high temperature atmosphere. And the carboxyl group in NA were bonded with the amino group in heptazine ring through thermal polymerization, then copolymerization to form UCNNA [33]. The crystalline structure of the samples was analyzed by X-ray diffraction (XRD). The XRD pattern in Fig. 1b shows a typical carbon nitride phase in all the prepared catalysts. The two diffraction peaks at 12.7° and 27.3° were well-indexed as the (100) and (002) planes, which corresponded to the in-plane repeated heptazine units and interlayer stacking of the conjugated aromatic structure, respectively

[34]. Additionally, the unchanged (002) peak position and the intensity decreased, indicating that NA was successfully grafted into the edge of UCNNA without changing their crystalline structure. The microstructure and morphology of catalysts were characterized by scanning electron microscopy (SEM) and transmission electron microscopy (TEM) imaging. As shown in Fig. 1c-d, the UCNNA40 exhibits a loose and broken morphology in contrast to PCN with a smooth surface. Comparing Fig. 1f and g, it is clear that UCNNA40 has a reduced degree of edge regularity and a coral-like morphology, which favors enhanced surface area and active site exposure. Furthermore, the C, N, and O elemental mapping were uniformly distributed throughout the UCNNA40 (Fig. 1e), further indicating the successful synthesis of the target catalysts.

To further identify the molecular structure of prepared samples, Fourier transform infrared (FT-IR) spectra as shown in Fig. 2a. All the PCN and UCNNA samples preserved the characteristic peaks within the aromatic C-N heterocycle induced a wide band (1200 cm^{-1} - 1720 cm^{-1}) and the signal of triazine units at 811 cm^{-1}, indicating the well-preservation of the fundamental carbon nitride structure in these catalysts [23]. Interestingly, the characteristic peaks of carbonyl group stretching vibration cannot be found in the FT-IR spectrum of UCNNA, which was likely induced by the overlap of C=O and C=N stretching vibration as well as the low content of C=O [35,36]. The elemental chemical states of the PCN and UCNNA40 were identified by X-ray photoelectron spectra (XPS) in Fig. 2b-f, and corrected by the C 1 s (284.80 eV). The PCN is mainly consisted of C and N, with a slight
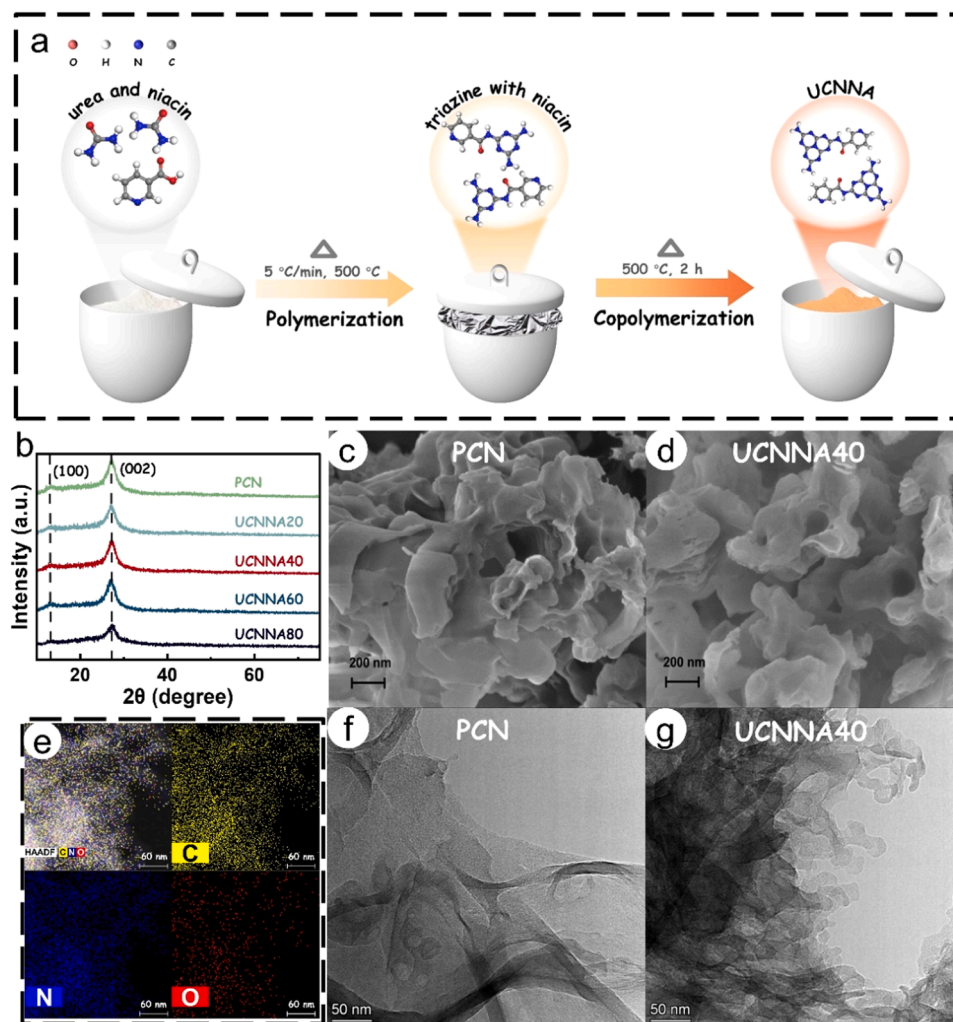

Fig. 1. (a) The possible polymerization reaction schematic of UCNNA sample. (b) The XRD pattern of the PCN and the UCNNA samples; the SEM image of (c) PCN and (d) UCNNA40; (e) the elemental mapping of UCNNA40; the TEM image of (f) PCN and (g) UCNNA40.
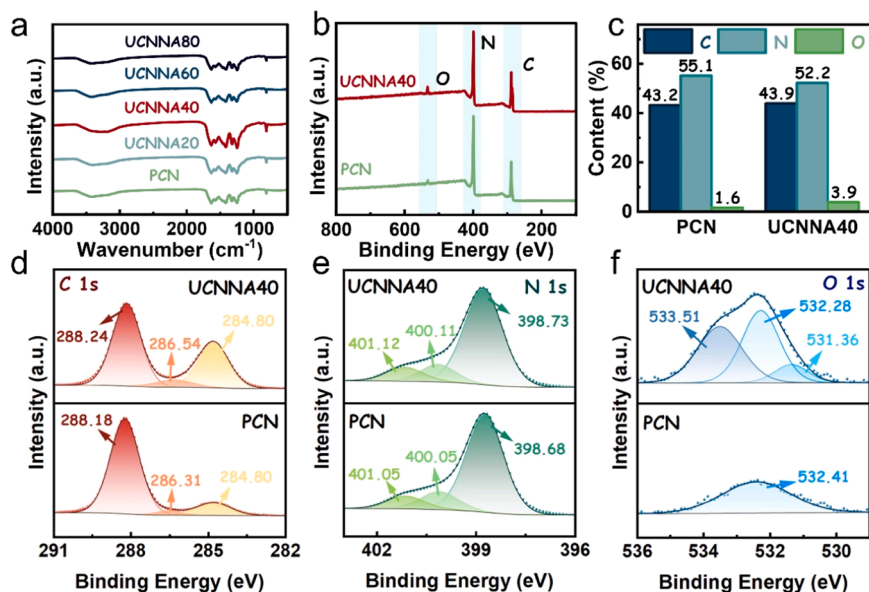
Fig. 2. (a) The FT-IR spectra of the PCN and the UCNNA samples. (b) The XPS survey, (c) the elementary contents of PCN and UCNNA40. (d) The C 1 s, (e) the N 1 s, and (f) the O 1 s spectra of PCN and UCNNA40.

amount of O (1.6%), referring to the adsorbed H_2O and CO_2 [37]. Owing to the introduction of NA, there are more O and C in the UCNNA40 than in the PCN (Fig. 2c). The narrow spectra of PCN and UCNNA40 were compared. As displayed in Fig. 2d, the chemical state of C 1 s in PCN mainly consists of 284.80 eV (C=C/C-C), 288.24 eV (N = C-N), and 286.54 eV (C-O/C=O) [38]. The peak areas of C=C/C-C and C-O/C=O for UCNNA40 are higher than that of PCN, which can be attributed to the C=O and pyridine rings in NA, further indicating the successful synthesis of the target catalysts [27]. The XPS of N 1 s spectrum (Fig. 2e) shows three peaks at 398. 68 eV, 400.05 eV, and 401.05 eV, which can be ascribed to the sp^2 hybridized nitrogen (C-N = C/N = C-N), tertiary

nitrogen (N-C$_3$), and terminal amino groups (-NH$_2$), respectively [34]. Notably, the binding energy of N-C$_3$ and -NH$_2$ peaks were upshifted in UCNNA40 compared to the PCN. This is ascribed to the enhanced electron density of the N atoms in UCNNA40 [24], raised from NA introduced into the structure. The C 1 s and N 1 s spectra of UCNNA40 were similar, demonstrating that the carbon nitride framework was not changed after the introduction. The difference between PCN and UCNNA40 is found from the O 1 s XPS spectrum (Fig. 2f), where UCNNA40 shows a more obvious peak than that of PCN. Besides the adsorbed oxygen (532.28 eV and 533.51 eV), a prominent peak assigning to C=O is found located at 531.36 eV, suggesting the NA
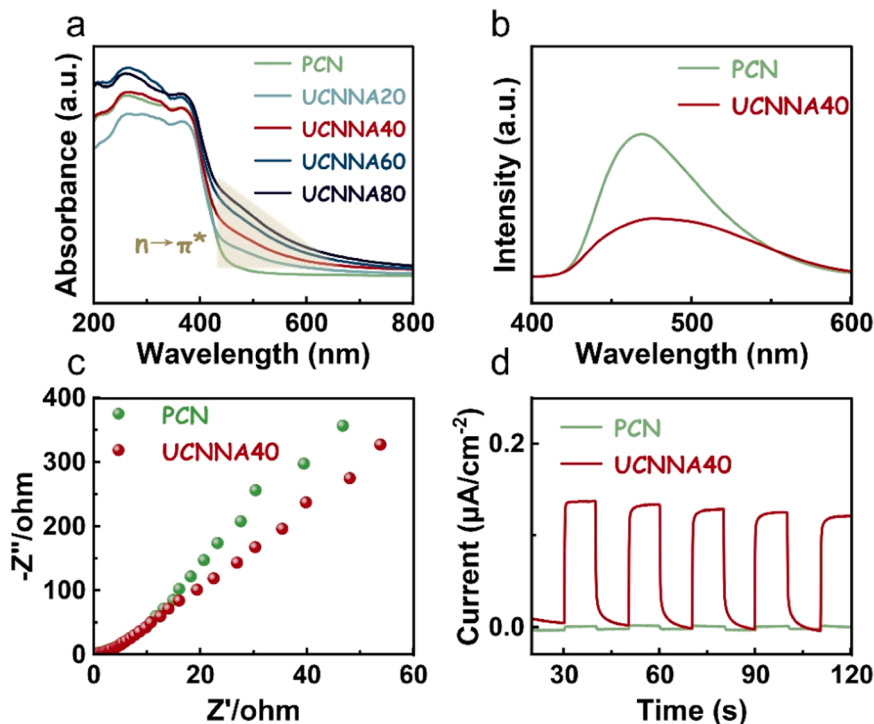

Fig. 3. (a) The UV–vis DRS spectra of the PCN and the UCNNA samples. (b) The PL spectra, (c) EIS Nyquist plots, and (d) transient photocurrent response of the PCN and UCNNA40.

introduced into the UCNNA40 [39].

In order to investigate the light absorption capacity, the diffuse reflectance spectra (DRS) were conducted. As depicted in Fig. 3a, UCNNA exhibits an n→π * electron transition within the 420–700 nm range. With the increase in NA content, the n→π * electron transition becomes more pronounced in the UCNNA samples [34]. This phenomenon can be attributed to the presence of a C═O group in NA, which functions as a chromophore [27]. Furthermore, NA can also disrupt the planar structure of PCN. The photophysical characteristics of photocarriers in different catalysts were evaluated using Photoluminescence (PL) spectra (Fig. 3b). Compared with PCN, the UCNNA shows a lower emission PL curve intensity, attributed to its excellent photocarrier separation capability. The NA serves as an electron acceptor group, altering the photocarrier transport properties of the PCN upon grafting. Subsequently, the charge separation efficiency of the catalysts under visible light was further analyzed by the electrochemical impedance spectroscopy (EIS) and transient photocurrent response. The results indicate that UCNNA exhibits a lower slope than PCN (Fig. 3c), suggesting a weaker charge transfer resistance. The transient photocurrent response in the catalysts was consistent with that observed in EIS, indicating a much higher photocurrent for UCNNA compared to PCN (Fig. 3d). Consequently, NA grafting can enhance the light utilization efficiency of PCN and reduce photocarrier recombination.

3.2. Overall ATZ degradation in the UCNNA/PMS/vis process

Herein, ATZ has been adopted to assess the photocatalytic activity of the UCNNAX/PMS/vis process. After 20 min of adsorption, PMS and light were introduced to initiate the catalytic reaction. The removal rates of ATZ by UCNNA20, UCNNA40, UCNNA60, and UCNNA80 reach 90%, 95%, 88%, and 71%, respectively (Fig. 4a). In addition, UCNNA40 exhibits the highest photocatalytic activity with a first order rate constant (k) of 0.050 min^{-1} compared to PCN (0.017 min^{-1}) (Fig. S1a). Given the best performance of the UCNNA40, the rest experiment was carried out by UCNNA40 (All the UCNNA mentioned below are UCNNA40). Fig. 4b illustrates the variations of ATZ concentration (C/C$_0$) with the time in the PMS/vis, UCNNA/vis, UCNNA/PMS/vis, and UCNNA/PMS/dark systems. PMS can hardly be activated by single UCNNA or single visible light to remove ATZ. Comparatively, the UCNNA can be excited and produce electron-hole pairs in the UCNNA/vis system, exhibiting 44%

ATZ removal. However, once PMS was introduced, the degradation efficiency of ATZ significantly rose to 95%. As mentioned above, the findings showed that the combination of PMS with the photocatalytic system (UCNNA/vis) had a significant synergistic impact. The pseudo-first-order-kinetics curves and pseudo-first order rate constants were shown in Fig. S1, the k of UCNNA/vis, PMS/vis, UCNNA/PMS/dark, and UCNNA/PMS/vis processes were 0.010 min^{-1}, 0.001 min^{-1}, 0.002 min^{-1}, and 0.050 min^{-1}, respectively. It was evident that the k of UCNNA/PMS/vis process, which was 5 times greater than that of the conventional UCNNA/vis process, was much higher than that of other processes.

The effects of catalyst concentration, PMS concentration, and ATZ concentration on ATZ degradation were examined. Within the range of 0.2 g/L-0.8 g/L catalysts concentration, the ATZ degradation efficiency increased from 87% to 98% (Fig. 4c). However, no discernible increase in ATZ degradation was seen until the catalyst concentration reached 0.4 g/L (Fig. S1c). Similarly, increasing the PMS concentration from 0.06 g/L to 0.6 g/L also remarkably promoted ATZ degradation, but the uptrend was insignificant when the additive PMS was over 0.2 g/L (Fig. 4d and S1d). Additionally, the effect of ATZ concentration was assessed (Fig. 4e). When the initial concentration was 8 mg/L and 10 mg/L, the ATZ removal respectively reached 97% (k = 0.058 min^{-1}) and 95% (k = 0.050 min^{-1}). With the initial concentration further decreased to 4 mg/L and 6 mg/L, 100% ATZ can be eliminated within 60 min. Obviously, with a concentration of 2 mg/L, 100% ATZ can be eliminated within 40 min, with greatly improved k (0.129 min^{-1}) (Fig. S1e). For the next trials, the catalyst dose and PMS concentration were set at 0.4 g/L and 0.2 g/L, respectively, taking into account the trade-off between costs and ATZ degradation performance.

Whether it can be applied in a wide pH is one of the crucial parameters to estimate the practical application prospect of water treatment technology. Thus, it is necessary to investigate the degradation effect of the UCNNA/PMS/vis system on ATZ at different pH. As shown in Fig. 4f, this system exhibited an excellent ATZ removal efficiency over a wide pH range (pH=3–9). The degradation efficiency significantly improved under acidic aqueous. At initial pH= 3.22, the ATZ removal was 98% within 60 min, with a higher k value of 0.093 min^{-1} (Fig. S1f). The final pH values of pH= 7.32 and pH= 9.13 after the reaction were displayed in Table S1. In the reaction systems with pH value of 7 to 9, the solution pH after reaction reduced to acidic. When the solution is
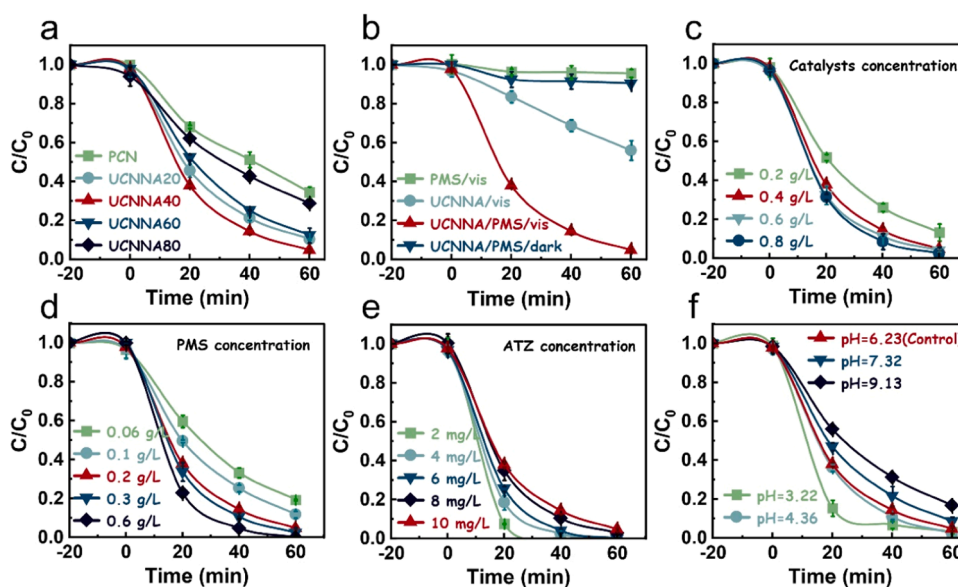

Fig. 4. (a) The influence of NA contents on ATZ degradation by UCNNA photocatalysis-activated PMS. (b) The removal variations of ATZ by different reaction processes. The photocatalysis-activated PMS efficiency for ATZ removal with different (c) catalysts concentration, (d) PMS concentration, (e) ATZ concentration, and (f) pH values.

moderately acidic, HSO_5^- was the predominant existence form of PMS and was activated by UCNNA [13]. As the initial pH reached 9, PMS primarily presented in the form of SO_5^{2-} (with the weaker catalytic activity), hindering the ATZ removal [40]. Overall, this broad pH adaptation (pH=3–9) suggested that the UCNNA/PMS/vis system was promising for practical applications.

3.3. Mechanism study

In photo-activating PMS systems, the pollutant removal can be achieved in two main pathways: radical pathway and non-radical pathway. The production of active species in the UCNNA/PMS/vis system was probed by employing scavengers (MeOH, TBA, EDTA-2Na, and p-BQ). Basically, the methanol (MeOH) could scavenge ·OH (k = 9.7 $\times 10^8$ $M^{-1} \cdot s^{-1}$) and ·SO_4^- (k = 2.5 $\times 10^7$ $M^{-1} \cdot s^{-1}$) simultaneously, while tert-butanol (TBA) could only scavenge ·OH (k·OH =(3.8–7.6) $\times 10^8$ $M^{-1} \cdot s^{-1}$ > k·SO_4^- = (4.0–9.1)$\times 10^5$ $M^{-1} \cdot s^{-1}$) [41]. In UCNNA/PMS/vis system, it was shown that ATZ degradation efficiency dropped from 95% to 75% in the presence of MeOH (100 mM) while the k dropped from 0.050 min^{-1} to 0.023 min^{-1} after the reaction for 60 min (Fig. 5a and S2a). In the presence of TBA (100 mM), the ATZ degradation efficiency dropped from 95% to 75% in the presence of TBA (100 mM), and k values ranged from 0.050 min^{-1} to 0.025 min^{-1} (Fig. 5b and S2b). The TBA and MeOH showed similar inhibitory effects on the UCNNA/PMS/vis system, indicating that·SO_4^- has a very weak effect. The ESR results also proved the existence of ·OH but the absence of ·SO_4^-. A representative four-line spectrum (1:2:2:1) was observed by Fig. 5c, demonstrating the generation of active ·OH during the reaction system. In addition, the peak of DMPO-·SO_4^- did not shown even after 20 min light exposure, this phenomenon might be caused by the quick transformation of ·SO_4^- to ·OH (Eq.1) [29,42]. These results indicated that ·OH had a limited role in the UCNNA/PMS/vis system.

$$\bullet SO_4^- + H_2O \rightarrow HSO_4^- + \bullet OH \tag{1}$$

It is worth mentioning that the enhancement of ATZ degradation during the first 20 min (Fig. 5d) was possibly contributed by the activation of PMS by p-BQ [43,44]. Therefore, the use of p-BQ was not appropriate for the $\bullet O_2^-$ identification in this case. The ESR experiment has been used to verify the presence of $\bullet O_2^-$ in the reaction. The intensity of the DMPO-$\bullet O_2^-$ in the UCNNA/PMS//vis system, indicating that the $\bullet O_2^-$ was produced in this system (Fig. 5g). More strikingly, the presence of 10 mM-100 mM EDTA-2Na and FFA all produce an obvious inhibition on the ATZ degradation (Fig. 5e-f). The k values for ATZ degradation in the UCNNA/PMS/vis system with 100 mM EDTA-2Na and 100 mM FFA were respectively 0.002 min^{-1} and 0.001 min^{-1} (Fig. S2c-d). This result implies that mainly h^+ and $^1O_2$ were response for ATZ degradation. The generation of $^1O_2$ during the reaction can be reflected by the concentration change of 9,10-dimethylanthracene (DMA) in the solution. The DMA could selectively react with $^1O_2$ to form endoperoxide (DMA-O_2), resulting in the decrease of solution absorbance [45]. As shown in Fig. S3a, it can be found that DMA maintains a stable absorbance after 5 min visible light irradiation. The absorbance of the DMA with the solely PMS or UCNNA addition exhibits a slight reduction (Fig. S3b and c). The DMA absorbance decreases constantly from light 1 min to 5 min after the simultaneous introduction of UCNNA and PMS (Fig. S3d). Moreover, the triplet spectrum with intensities 1:1:1 indicated TEMP-$^1O_2$ adduct signal (Fig. 5h), and its intensity greatly increased after 10 min or 20 min reaction, suggesting that $^1O_2$ was continuously being produced in the UCNNA/PMS/vis system. Both the DMA specific probe test and ESR experiment results proved that $^1O_2$ is an important reactive oxygen species in the system.

It is necessary to further reveal the pathway of $^1O_2$ production. It is reported that the following reaction might result in the production of $^1O_2$ (Eqs. 2–5). Given the low efficiently of generating $^1O_2$ during the PMS self-decomposition, which indicated that the contribution of Eq. (2)
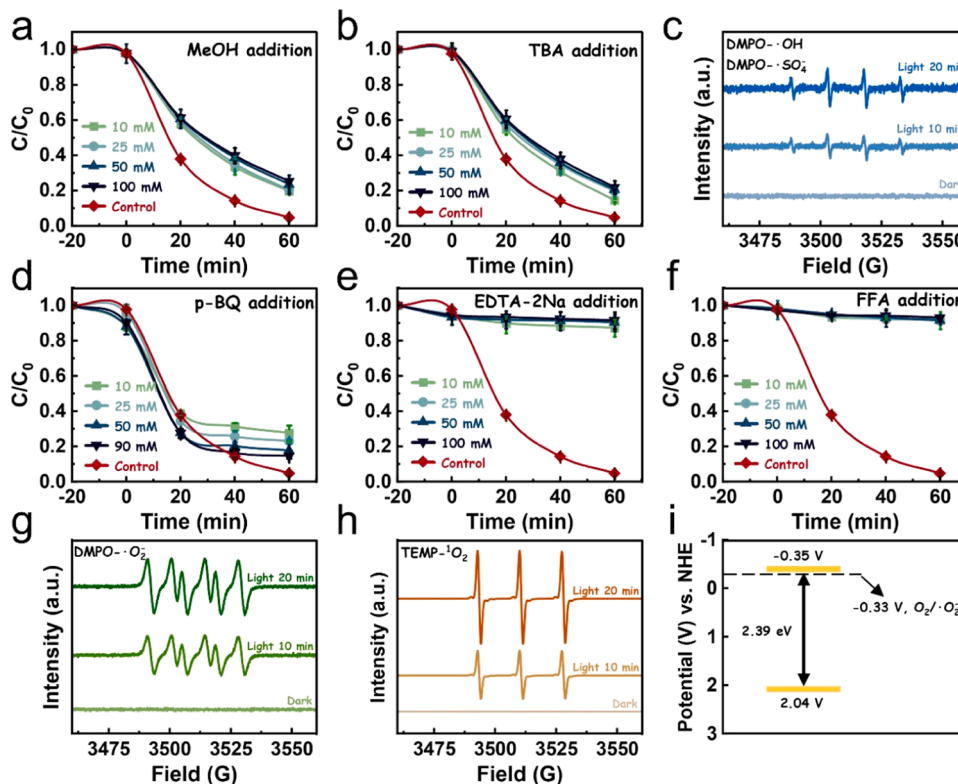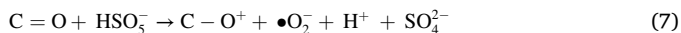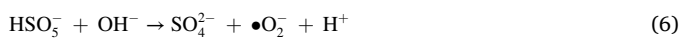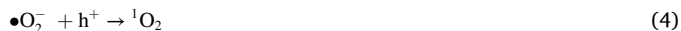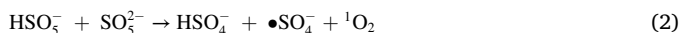

Fig. 5. The effect of (a) MeOH, (b) TBA, (d) p-BQ, (e) EDTA-2Na, and (f) FFA with different concentration on the degradation of ATZ by UCNNA/PMS/vis process. The ESR results of (c) ·OH and $\bullet SO_4^-$ (g) $\bullet O_2^-$, and (h) $^1O_2$ in the darkness and visible light 10 min, and 20 min (i) The illustration of the electronic band structure of UCNNA.

may be disregarded. The $\bullet O_2^-$ is an important precursor for the production of $^1O_2$, which inferred that most of $^1O_2$ were converted from $\bullet O_2^-$ (Eqs. 3 and 4). In addition, previous studies have also mentioned the possible participation of O_2 in the production of $\bullet O_2^-$ [46]. To understand the oxidation and reduction capacity of the UCNNA, the bandgap and valence band (VB) information was acquired (Fig. S4a and b). According to the calculated results, the CB and VB of UCNNA is estimated to be -0.35 V and 2.04 V [47,48]. The electron configuration of the UCNNA was described in Fig. 5i. Given the electronic band structure discussed and the redox potential for $O_2/\bullet O_2^-$ (-0.33 V) conversion [37,49], it should be possible for the production of the $\bullet O_2^-$ via reducing O_2 (Eq. 5). To verify this assumption, continuous N_2 was pumped into UCNNA/PMS/vis system to eliminate dissolved oxygen during the reaction (Fig. S5). There is no distinct difference in the final removal efficiency, thus indicating that O_2 is not the major contributor to the generation of the $\bullet O_2^-$ (Eq. 5). In previous studies, the PMS activation process could lead to the generation of $\bullet O_2^-$ [50]. UCNNA could be a catalyst, facilitating the activation of PMS for the formation of $\bullet O_2^-$. The plausible process is proposed as shown in Eq. 6 [51,52]. In addition, the PMS can be adsorbed on the catalyst surface through C=O groups to generate $\bullet O_2^-$ (Eq. 7). These results demonstrated a non-radical active system dominated by $^1O_2$ in UCNNA was generated from activation of PMS.

$$HSO_5^- + SO_5^{2-} \rightarrow HSO_4^- + \bullet SO_4^- + {}^1O_2 \quad (2)$$

$$\bullet O_2^- + \bullet OH \rightarrow OH^- + {}^1O_2 \quad (3)$$

$$\bullet O_2^- + h^+ \rightarrow {}^1O_2 \quad (4)$$

$$e^- + O_2 \rightarrow \bullet O_2^- \quad (5)$$

$$HSO_5^- + OH^- \rightarrow SO_4^{2-} + \bullet O_2^- + H^+ \quad (6)$$

$$C=O + HSO_5^- \rightarrow C-O^+ + \bullet O_2^- + H^+ + SO_4^{2-} \quad (7)$$

Generally, the generation of reactive oxygen species correlates with electron-transfer (the gain and loss of electrons) during the oxidation process [53]. Therefore, it was necessary to investigate the electron-transfer behavior in UCNNA/PMS/vis system. At the beginning, the involved solution-phase electrons are likely scavenged by K_2CrO_4 to result in inhibited $\bullet O_2^-$ generation as well as substrate degradation [54,55]. As shown in Fig. S5b, ATZ degradation was slightly inhibited in UCNNA/PMS/vis upon K_2CrO_4 addition. Combine the result of Fig. S5a, suggesting that a small percentage of $\bullet O_2^-$ are derived from the solution-phase electrons reaction with oxygen. Therefore, the system is likely based on direct electron transfer on the catalyst surface. With the help of linear sweep voltammetry (LSV) and chronoamperometric i-t curve analysis, it was possible to better understand how electrons transfer between ATZ, catalysts, and PMS. The addition of ATZ had no effect on the chronoamperometric current, indicating that no electron transfer occurred between UCNNA and ATZ. When the PMS and ATZ were successively injected the current output was significantly enhanced (Fig. 6a). These observations indicate that after the electron-transfer, the "metastable reactive complex" was possibly formed, thereby resonating with the LSV results. In Fig. 6b, the current density in the LSV curves increased with the presence of PMS, and the addition of ATZ provided some electrons to accelerate the reaction, thus inducing the current increase further. These results imply that the formation of "metastable PMS/UCNNA surface complex" was a crucial step in the generation of highly reactive species. The electron-transfer pathway was explored by DFT calculations [56]. Here, the LUMO of UCNNA (-2.460 eV) was more negative than the LUMO of ATZ (-0.611 eV), implying that the electrons at the LUMO of ATZ can be easily transferred to the LUMO of UCNNA. Meanwhile, the gap between the HOMO and LUMO of UCNNA (4.16 eV) was smaller than PCN (4.99 eV), implying that the lower energy barrier of UCNNA facilitates an easier electron migration from the HOMO to the LUMO (Fig. S6). Then, the LUMO of UCNNA (-2.460 eV) is closer to the LUMO of PMS (-2.810 eV) than PCN (-1.258 eV), suggesting that electrons on UCNNA readily leap into PMS, thus activating PMS more rapidly (Fig. 6c). To investigate the adsorption behaviors of PMS on PCN and UCNNA surfaces, the adsorption energy for PMS adsorption on PCN and UCNNA was calculated by DFT (Fig. 6d). In UCNNA, the NA groups grafted on the surface have much higher adsorption energy (-1.58 eV) than heptazine ring (-0.44 eV) or PCN (-0.50 eV) (Fig. 6e). This implies that the electron acceptor NA groups function as adsorption sites for PMS.

Derived from the above consequences, the possible mechanism of PMS photocatalytic activation over the UCNNA for the ATZ degradation
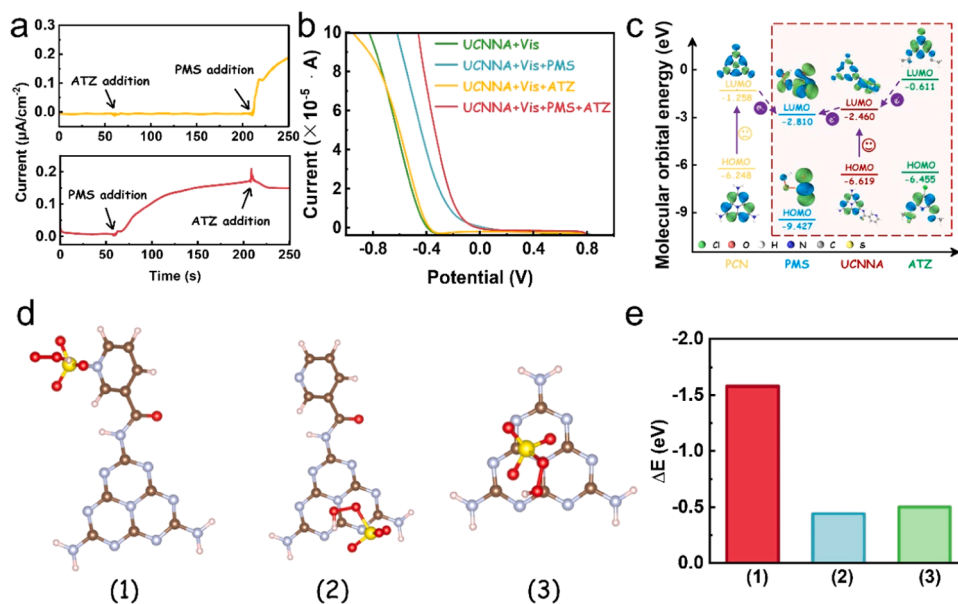

Fig. 6. (a) Chronoamperometric i-t curves were obtained with 0.2 M Na_2SO_4 as the electrolyte under different PMS and ATZ addition sequences. (b) LSV curves variations after the subsequent additions of ATZ or/and PMS. (c) Electron transfer pathways during ATZ degradation. (d) Adsorption models on NACN and PCN and (e) corresponding binding energies.

was proposed. As shown in Scheme 1, under the visible light irradiation, the electrons clustered on NA groups that acted as electron acceptors, effectively preventing the recombination of photogenerated carriers in-plane. Concurrently, PMS adsorbed onto the NA groups, facilitating electron transfer to PMS and activating it to generate $^1O_2$. Additionally, the $\bullet O_2^-$ reacted with the h^+, resulting in the formation of $^1O_2$. Ultimately, the concerted actions of $^1O_2$ and electron transfer contribute to the removal of ATZ.

3.4. Stability and reusability of the UCNNA/PMS/vis system

In natural water, some unavoidable coexisting substances, such as natural organic matters (NOM), low molecular weight organic acids (LMWOA), and inorganic anions, may interfere with the PMS activation system. Therefore, it is necessary to understand the effect of interfering substances on the UCNNA40/PMS/vis process. Humic acid (HA), citric acid (CA), fulvic acid (FA), and oxalic acid (OA) were selected as typical NOM and LMWOA to analyze the influence on ATZ degradation. The UCNNA40/PMS/vis process showed superior compatibility with NOM and LMWOA (Fig. 7a-d). Besides, a series of coexisting ions including NO_3^-, SO_4^{2-}, Cl^-, CO_3^{2-}, and HCO_3^- with different concentrations were representatively added into the UCNNA40/PMS/vis system. The negligible effects of NO_3^- and SO_4^{2-} on the UCNNA40/PMS/vis system were observed even at an initial 10 mM anion concentration (Fig. 7e and f). By contrast, the k rose sharply to 0.083 min^{-1}-0.101 min^{-1} with the existence of Cl^- (Fig. 7g and Fig. S7g). The acceleration of ATZ in this system is likely resulting from the generation of HClO, which has a relatively high oxidation ability (Eq. 8) [57]. Nevertheless, the CO_3^{2-} and HCO_3^- injection reduced the ATZ degradation efficiency (Fig. 7h and i). The changes from the addition of CO_3^{2-} and HCO_3^- were mainly attributed to two reasons: (1) the base environment via their hydrolysis; (2) the competing reactions between CO_3^{2-} or HCO_3^- with PMS at the catalyst surface [30,58].

$$HSO_5^- + Cl^- \rightarrow SO_4^{2-} + HClO \qquad (8)$$

Besides, to further estimate the potential practicality of UCNNA/PMS/vis system, the comparison was operated with the contaminated water, including tap water and river water (Liuyang River). As shown in Fig. S8a and b, in wastewater solution (containing a large number of NOMs, inorganic anions, biomass, and LMWOAs), the UCNNA/PMS/vis system can remove 80% of high concentration ATZ, while more than 90% of low concentration ATZ can be removed. Thus, the UCNNA/PMS/vis system shows excellent promise for effective wastewater treatment. In addition, the UCNNA/PMS/vis system was applied for the degradation of multiple organic pollutants, such as ciprofloxacin (CIP), sulfamethazine (SMT), imidacloprid (IMD), and clothianidin (CLT). Fig. S8c depicted the removal ratio of multiple organic pollutants in UCNNA/PMS/vis system after 60 min reaction. The degradation efficiency changes depend on different kinds of organic pollutants. The degradation ratios of CIP, SMT, IMD, and CLT in the UCNNA/PMS/vis system were 100%, 100%, 72%, and 65% after 60 min reaction. All these results indicated the UCNNA/PMS/vis system can not only degrade antibacterial compounds and antibiotics but also can effectively degrade neonicotinoid insecticide. In conclusion, the UCNNA/PMS/vis system has excellent and potential properties for organic pollutants degradation.

Moreover, a four-cycle recycling test was performed to evaluate the reusability and potential practicality of UCNNA towards PMS activation (Fig. S8d). After four rounds of degradation experiments, the ATZ removal rate in UCNNA/PMS/vis system is basically stable (97%, 93%, 91%, and 87%), slightly lower than the first cycle. At last, the XRD and XPS spectra were selected for revealing the stability of UCNNA structure. As shown in Fig. S9a, the crystal structure did not show obvious charge. Besides, the peak of XPS spectrum of the UCNNA hardly changed before and after the cycles (Fig. S9b-d). The removal rate and the reaction rate constant for ATZ in various studies are compiled in Table S2 [59–63]. Despite not having the highest removal rate, when factoring in reaction time and economic cost, the reaction constant of the UCNNA/PMS/vis system is outstanding.
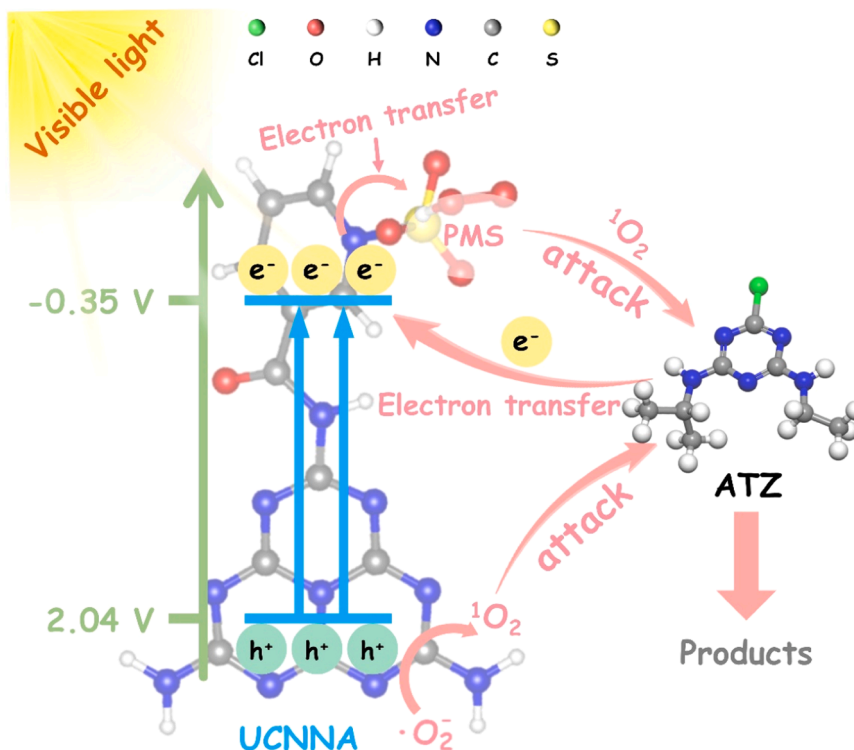
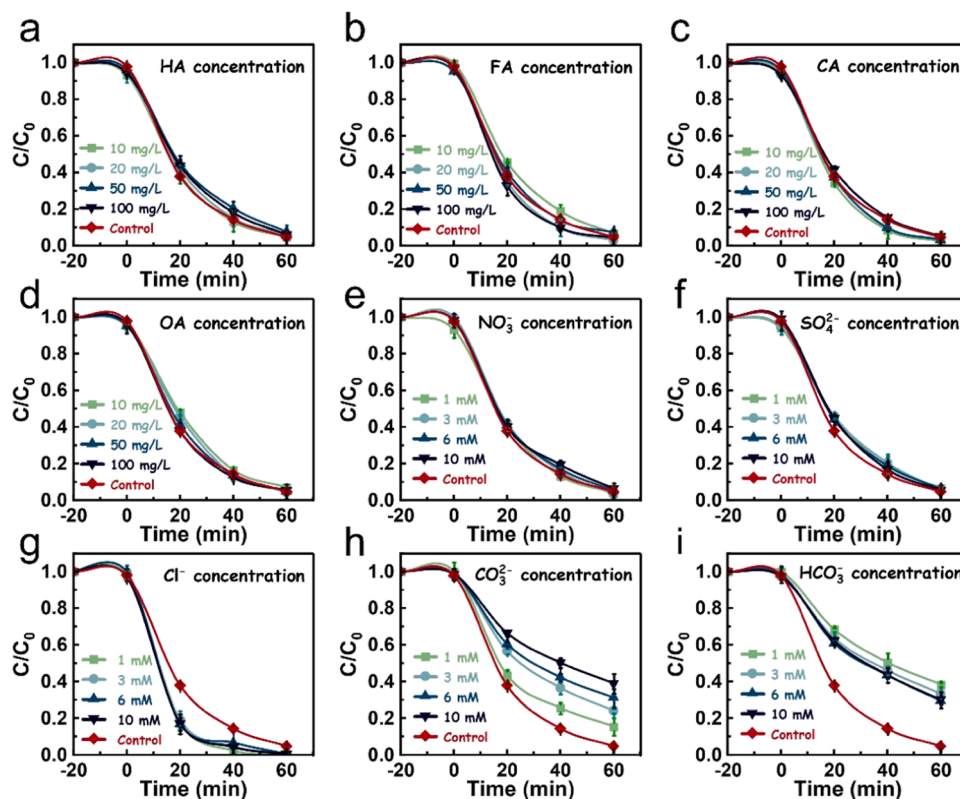**Scheme 1.** Mechanism of PMS activation and ATZ degradation on UCNNA.

Fig. 7. The effect of (a) HA, (b) FA, (c) CA, (d) OA, (e)NO_3^-, (f) SO_4^{2-}, (g) Cl^-, (h) CO_3^{2-}, and (i) HCO_3^- with different concentration on the degradation of ATZ by UCNNA/PMS/vis process.

3.5. Identification of ATZ degradation products and possible pathways

The LC-MS was applied to identify intermediates generated in UCNNA/PMS/vis system during the ATZ degradation, and the corresponding MS spectra were provided in Figs. S10-S14. Based on the m/z identified by LC-MS, 14 possible major intermediates were detected and the data for these intermediates was summarized in Table S3. Besides, the Fukui index of ATZ molecule was applied to predict the active sites (Fig. 8). The optimized chemical structure of the ATZ is shown in Fig. 8a. Theoretically, the higher electrophilic (f-), nucleophilic (f+), and radical (f0) values of ATZ atom refer to an easier by electrophilic species ($^1O_2$ and h^+), nucleophilic species ($\bullet O_2^-$), and radical species ($\cdot SO_4^-$ and $\cdot OH$) attacks (Fig. 8b-e) [64]. The involvement of $^1O_2$ and h^+ in UCNAN/PMS/vis system is highlighted in the discussion above, which could degrade ATZ by electrophilic attack. As shown in Fig. 8b and c, the 2 N (0.1297), 1 N (0.1254), 5 N (0.1007), and 4 N (0.0849) positions exhibited high f- values, suggesting the potential for $^1O_2$ and h^+ attack. However, the saturated bonds and higher steric hindrance resulted in the high stability of the above-mentioned atoms, and can hardly be attacked by $^1O_2$ and h^+ [65,66]. Combining orbital analysis, the HOMO was located on the lateral chain of ATZ, suggesting the regions easily escape electrons, which would be attacked by $^1O_2$ and h^+. Therefore, 9 C and 12 C were prone to being attacked by electrophilic $^1O_2$ and h^+. Besides, 14Cl with higher f+ (0.1587) and f0 (0.1319) index might be replaced by the OH group. To make the proposed degradation pathways more plausible, the Fukui functions of possible intermediates are calculated (Figs. S15-S27). These analyses were used with literature research [67], suggesting three possible ATZ degradation pathways, i.e., lateral chain oxidation (Pathway I and II) and dichlorination-hydroxylation (Pathway III) (Fig. S28).

Pathway I mainly involved the dealkylation, alkylic-oxidation, and deamination-hydroxylation process. The hydrogen atoms on the 9 C are electrophilically attacked (by $^1O_2$ or h^+) and oxidized to the C=O group

(P-1, $m/z = 230$). Then the P-1 transformed into P-2 ($m/z = 188$) by the removal of isopropyl group as a result of the f- (0.1007) value of 5 N [68]. P-2 further underwent dealkylation and hydroxylation to produce the intermediate P-3 ($m/z = 190$) and P-4 ($m/z = 148$) [69]. With the demethylation and deethylation on the triazine ring, the P-5 ($m/z = 136$) was formed. Besides, though pathway II is also lateral chain oxidation, it involves the lateral chain loss of ethyl group and the addition of the methyl group, before the dichlorination and dealkylation of the triazine ring. The first stage in pathway II was the demethylation in the lateral chain of the ATZ to produce P-6 ($m/z = 202$), followed by the elimination of the isopropyl group and alkylic-oxidation, which produced P-2 ($m/z = 188$) and P-7 ($m/z = 185$). The P-8 ($m/z = 146$) was produced via consecutive addition and dealkylation reactions of $^1O_2$ [69].

Comparatively, pathway III mainly originated from the dechlorination-hydroxylation, accompanied by the $^1O_2$ or h^+ attack on the lateral chain. First, the alkyl hydroxylation P-9 ($m/z = 232$) was formed by alkyl hydroxylation reaction. Based on the high f- value of 14Cl (0.1051) and the C-Cl band length (1.734 Å) was prone to rupture [5,70], thus the ATZ degradation could be initiated by dechlorination-hydroxylation and the Cl atom was replaced by -OH to generate P-10 intermediate ($m/z = 212$). Then, the P-10 experienced olefination, producing P-11 ($m/z = 183$). Subsequently, demethylation was successive happened to produce P-12 ($m/z = 170$), P-13 ($m/z = 155$), and the final intermediate P-14 ($m/z = 128$) [71,72]. By calculating the Fukui index of the intermediate products, it was found that the higher f- values are mainly distributed on the side chain of the intermediate product, which is consistent with the suggested three possible ATZ degradation pathways.

3.6. Toxicity assessment of intermediates

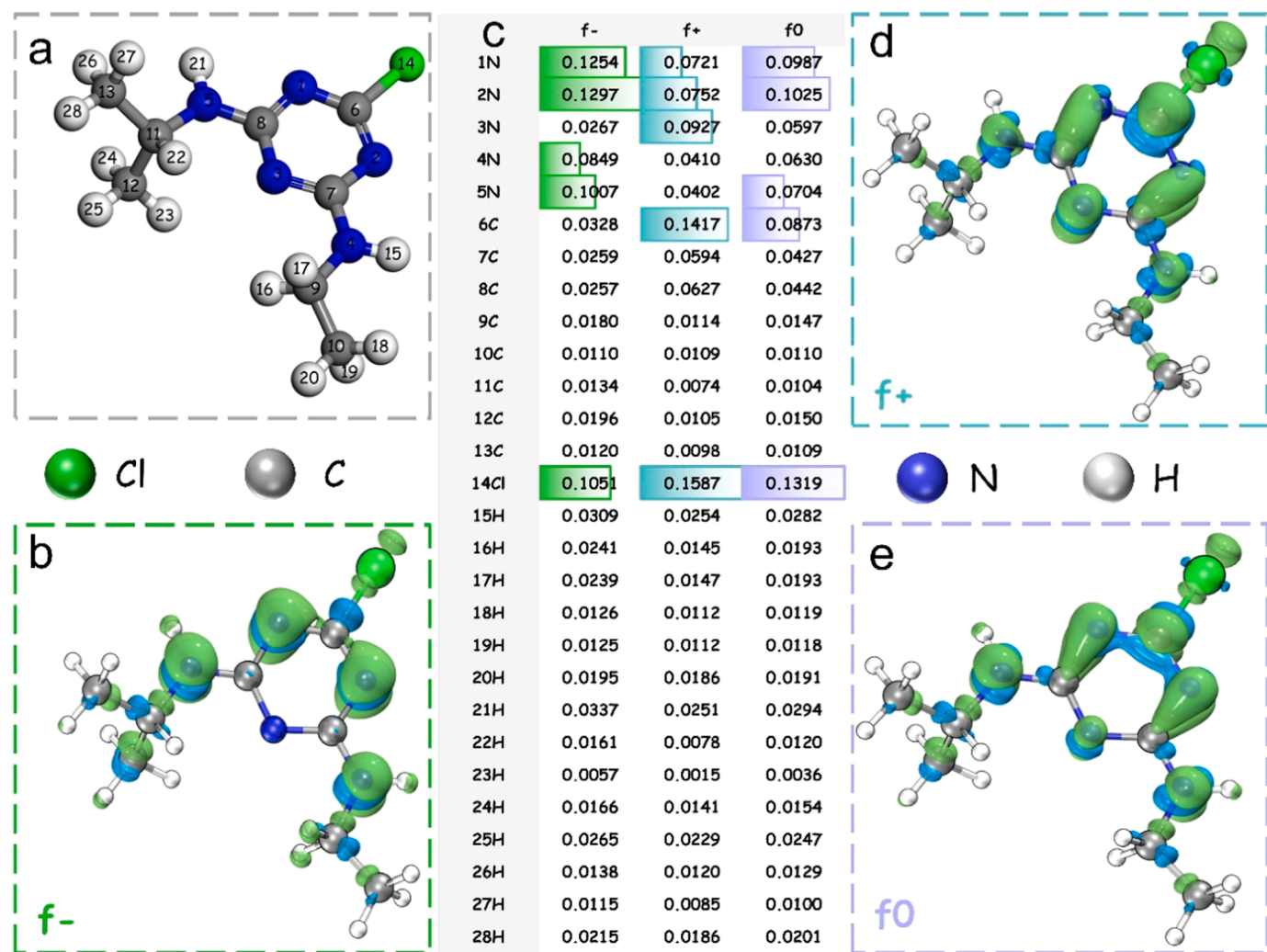The acute toxicity and bioaccumulation factor of ATZ and its

Fig. 8. (a) Chemical structure of ATZ after optimization with numbers marked. (c) The calculated Fukui index distribution on ATZ molecule, (b) f-, (d) f+ , and (e) f0 index isosurface on ATZ molecule.

degradation intermediates were well understood by utilizing the Toxicity Estimation Software Tool (T.E.S.T). The acute toxicity prediction value intensity of fathead minnow LC_{50} (96 h) and Daphnia magna LC_{50} (48 h) can be divided according to the Globally Harmonized System Classification and Labelling of Chemicals [73]. Meanwhile, the World Health Organization of the pesticides classification by hazard and guidelines recommended can be used to divide the rat oral LD_{50} [70]. Fig. 9a shows that practically all intermediates have substantially lower bioaccumulation factors than ATZ, with the highest decrease of 96.6% (P-12) and the lowest decrease of 29.8% (P-4). ATZ was categorized as moderately hazardous based on the acute toxicity prediction value intensity of the oral rat LD_{50}. Among the major 14 intermediates obtained, 8 intermediates (P-1, P-3, P-9, P-10, P-11, P-12, P-13, and P-14) were less toxic than ATZ, and 6 intermediates (P-3, P-9, P-10, P-12, P-13, and P-14) of them were slightly dangerous (Fig. 9b). Particularly, P-4, hazardous chemical, was the intermediate with the greatest damaging effect on rats, and it was more toxic than that of ATZ. Besides, the oral rat LD_{50} concentration value of P-14 was 3971 mg/kg, reaching the "no acute hazard" category. The toxicity of most intermediates was substantially lower than that of ATZ, and even near to non-toxic (>100 mg/L), based on the acute toxicity of Daphnia magna LC_{50} (48 h) and fathead minnow LC_{50} (96 h) (Fig. 9c and d). These prediction results indicated that ATZ could be degraded into low-toxic or non-toxic intermediates after the treatment of the UCNNA/PMS/vis system.

Furthermore, to directly represent the toxicity changes in the

degradation process, soybean culture experiments were carried out. Information about soybean culture experiment in support information (detailed culture process in Text S4, nutrient solution information in Table S4). The tri-leaf stage was weighed and chlorophyll extraction was carried out. Fig. S29a displayed that a few chlorophyll content was observed, on the nutrient solution with the addition of ATZ (photocatalytic treatment for 0 min), indicating that the ATZ had a strong inhibition effect on photosynthesis. However, the chlorophyll content gradually increased, after treatment with UCNNA/PMS/vis system. Compared with the blank group, the inhibition effect of ATZ with 60 min photocatalytic treatment on photosynthesis was negligible. The chlorophyll content of the T80 sample was 3.15 mg/g (the normal range of soybean chlorophyll content was 2.22 mg/g - 2.72 mg/g) [74], which was close to the value of blank group chlorophyll content (Fig. S29b), signifying that UCNNA/PMS/vis system can significantly degrade ATZ into less toxic intermediates after 80 min. This experimental phenomenon was consistent with the T.E.S.T results, indicating that the UCNNA/PMS/vis system is effective for ATZ removal and has promising potential in environmental remediation.

4. Conclusions

In summary, the UCNNA polymer was prepared by copolymerization of urea and NA. The introduction of NA as an electron acceptor group not only accelerates the photocarrier separation efficiency, but also
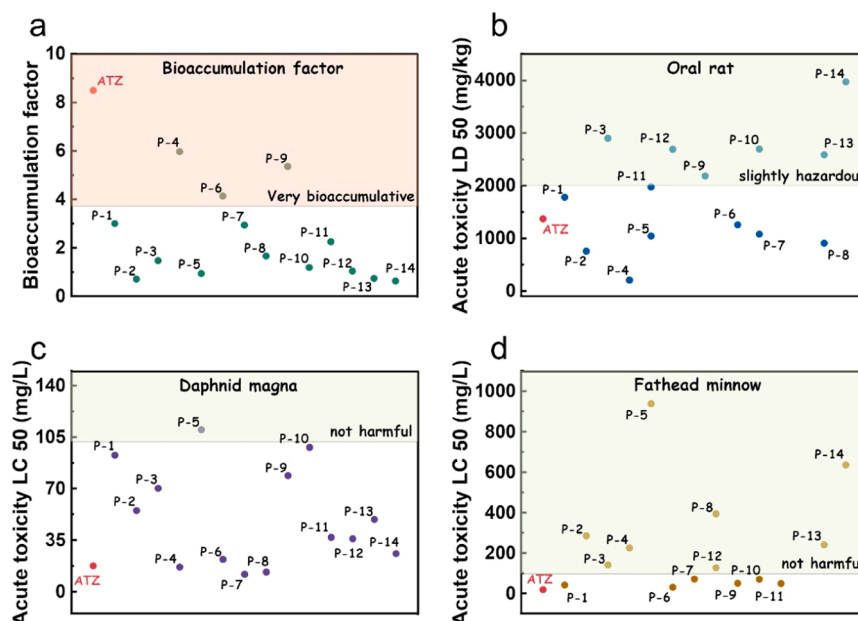
Fig. 9. (a) Bioaccumulation factor, and the acute toxicity of (b) oral rat LD$_{50}$, (c) Daphnia magna LC$_{50}$ (48 h), and (d) fathead minnow LC$_{50}$ (96 h) degradation intermediates of ATZ via T.E.S.T. (as the label for predicted value rather than experimental value).

improves the activation ability of PCN to PMS. The reaction rate constants of ATZ degradation with UCNNA/PMS/vis system dramatically enhanced to $5.0 \times 10^{-2} \cdot \text{min}^{-1}$, which is 2.9 times higher than the PCN/PMS/vis system. Both the DMA specific probe test and ESR experiment results proved that $^1O_2$ is an important reactive oxygen species in the system, and the primary pathway for $^1O_2$ generation involves the reaction between $\bullet O_2^-$ and h^+. Additionally, the formation of "metastable PMS/UCNNA surface complex" during the reaction induces a notable electron transfer behavior. Concurrently, the calculation of molecular orbital energy and PMS adsorption energy proved that NA not only serves as an electron acceptor to impede the recombination of photogenerated carriers in the plane, but also functions as an adsorption site for PMS to promote electron transfer and the generation of $^1O_2$. The characteristic of non-radical pathway enables UCNNA/PMS/vis system to maintain efficient ATZ degradation under the interference of various environmental factors. Furthermore, the 14 degradation intermediates and three possible degradation pathways of ATZ were inferred by calculating the Fukui index, combined with LC-MS analysis. The toxicity evaluation software and soybean culture experiments to elucidate the degradation process might successfully reduce pollutant environmental toxicity. This study verified that the UCNNA/PMS/vis system is an effective method for organic pollutants degradation, and the results provided new insights into green PMS activation strategies.

CRediT authorship contribution statement

Huang Ying: Resources, Funding acquisition. **Deng Yaocheng:** Writing – review & editing, Resources, Methodology, Funding acquisition, Conceptualization. **Li Wenbo:** Writing – review & editing. **Zhou Zhanpeng:** Writing – review & editing, Formal analysis. **Xiong Sheng:** Visualization. **Li Ling:** Writing – original draft, Validation, Investigation, Conceptualization. **Zeng Hao:** Software. **Tang Rongdi:** Writing – review & editing, Visualization, Resources.

Declaration of Competing Interest

The authors declare that they have no known competing financial interests or personal relationships that could have appeared to influence the work reported in this paper.

Data Availability

Data will be made available on request.

Appendix A. Supporting information

Supplementary data associated with this article can be found in the online version at doi:10.1016/j.apcatb.2024.123693.

References

[1] M.E. Taverna, C.A. Busatto, M.R. Lescano, V.V. Nicolau, C.S. Zalazar, G.R. Meira, D.A. Estenoz, Microparticles based on ionic and organosolv lignins for the controlled release of atrazine, J. Hazard. Mater. 359 (2018) 139–147.

[2] H. He, Y. Liu, S. You, J. Liu, H. Xiao, Z. Tu, A review on recent treatment technology for herbicide atrazine in contaminated environment, Int. J. Environ. Res. Public. Health 16 (2019) 5129.

[3] Q. Li, Y. Luo, J. Song, L. Wu, Risk assessment of atrazine polluted farmland and drinking water: a case study, B. Environ. Contam. Tox. 78 (2007) 187–190.

[4] W. Ouyang, G. Cai, M. Tysklind, W. Yang, F. Hao, H. Liu, Temporal-spatial patterns of three types of pesticide loadings in a middle-high latitude agricultural watershed, Water Res. 122 (2017) 377–386.

[5] C. Chen, S. Yang, Y. Guo, C. Sun, C. Gu, B. Xu, Photolytic destruction of endocrine disruptor atrazine in aqueous solution under UV irradiation: products and pathways, J. Hazard. Mater. 172 (2009) 675–684.

[6] G.Q. Saalfeld, A.S. Varela Junior, T. Castro, D.M. Pires, J.R. Pereira, F.A. Pereira, C.D. Corcini, E.P. Colares, Atrazine exposure in gestation and breastfeeding affects Calomys laucha sperm cells, Environ. Sci. Pollut. R. 26 (2019) 34953–34963.

[7] V. Soni, Sonu, A. Sudhaik, P. Singh, S. Thakur, T. Ahamad, V.H. Nguyen, L.P. Thi, H.H.P. Quang, V. Chaudhary, P. Raizada, Visible-light-driven photodegradation of methylene blue and doxycycline hydrochloride by waste-based S-scheme heterojunction photocatalyst Bi$_5$O$_7$I/PCN/tea waste biochar, Chemosphere 347 (2024) 140694.

[8] A.A.P. Khan, Sonu, A. Sudhaik, P. Raizada, M. Danish, A. Khan, T. Kamal, M.M. Rahman, A.M. Asiri, P. Singh, Fabrication of direct Z-scheme heterojunction of S

doped g-C$_3$N$_4$/Ag/AgI for efficient dye degradation, Mater. Lett. 357 (2024) 135666.

[9] V. Soni, Sonu, P. Singh, S. Thakur, P. Thakur, T. Ahamad, V.-H. Nguyen, Q. Van Le, C.M. Hussain, P. Raizada, Fabricating cattle dung-derived nitrogen-doped biochar supported oxygen-deficient ZnO and Cu$_2$O-based novel step-scheme photocatalytic system for aqueous Doxycycline hydrochloride mitigation and Cr (VI) reduction, J. Environ. Chem. Eng. 11 (2023) 110856.

[10] R. Kumar, A. Sudhaik, Sonu, V.-H. Nguyen, Q. Van Le, T. Ahamad, S. Thakur, N. Kumar, C.M. Hussain, P. Singh, P. Raizada, Graphene oxide modified K, P co-doped g-C$_3$N$_4$ and CoFe$_2$O$_4$ composite for photocatalytic degradation of antibiotics, J. Taiwan Inst. Chem. E 150 (2023) 105077.

[11] S. Patial, A. Sudhaik, Sonu, S. Thakur, Q. Van Le, T. Ahamad, P. Singh, C. W. Huang, V.H. Nguyen, P. Raizada, Synergistic interface engineering in n-p-n type heterojunction Co$_3$O$_4$/MIL/Mn-STO with dual S-scheme multi-charge migration to enhance visible-light photocatalytic degradation of antibiotics, Environ. Res. 240 (2024) 117481.

[12] R. Tang, H. Zeng, Y. Deng, S. Xiong, L. Li, Z. Zhou, J. Wang, L. Tang, Dual modulation on peroxymonosulfate activation site and photocarrier separation in carbon nitride for efficient photocatalytic organics degradation: Efficacy and mechanism evaluation, Appl. Catal., B. 336 (2023) 122918.

[13] J. Jing, X. Wang, M. Zhou, Electro-enhanced activation of peroxymonosulfate by a novel perovskite-Ti$_4$O$_7$ composite anode with ultra-high efficiency and low energy consumption: The generation and dominant role of singlet oxygen, Water Res. 232 (2023) 119682.

[14] S. Xiong, H. Zeng, R. Tang, L. Li, Z. Zhou, J. Wang, C. Ding, D. Gong, Y. Deng, Synergistic effect of high-valent cobalt oxo species and piezoelectricity on enhanced peroxymonosulfate activation for atrazine removal, Chem. Eng. J. 466 (2023) 143200.

[15] R. Ding, W.F. Yan, Y. Wu, Y. Xiao, H.Y. Gang, S.H. Wang, L.X. Chen, F. Zhao, Light-excited photoelectrons coupled with bio-photocatalysis enhanced the degradation efficiency of oxytetracycline, Water Res. 143 (2018) 589–598.

[16] R.L. Yin, B.H. Jing, S.X. He, J.Y. Hu, G. Lu, Z.M. Ao, C.Y. Wang, M.S. Zhu, Near-infrared light to heat conversion in peroxydisulfate activation with MoS$_2$: A new photo-activation process for water treatment, Water Res. 190 (2021) 116720.

[17] L. Li, X. Yuan, Z. Zhou, R. Tang, Y. Deng, Y. Huang, S. Xiong, L. Su, J. Zhao, D. Gong, Research progress of photocatalytic activated persulfate removal of environmental organic pollutants by metal and nonmetal based photocatalysts, J. Clean. Prod. 372 (2022) 133420.

[18] M. Cui, K. Cui, X. Liu, X. Chen, Z. Guo, Y. Chen, C.X. Li, Insights into the photocatalytic peroxymonosulfate activation over defective boron-doped carbon nitride for efficient pollutants degradation, J. Hazard. Mater. 418 (2021) 126338.

[19] S. Cao, J. Low, J. Yu, M. Jaroniec, Polymeric photocatalysts based on graphitic carbon nitride, Adv. Mater. 27 (2015) 2150–2176.

[20] J. Fan, H. Qin, S. Jiang, Mn-doped g-C$_3$N$_4$ composite to activate peroxymonosulfate for acetaminophen degradation: the role of superoxide anion and singlet oxygen, Chem. Eng. J. 359 (2019) 723–732.

[21] V. Hasija, V.H. Nguyen, A. Kumar, P. Raizada, V. Krishnan, A.A.P. Khan, P. Singh, E. Lichtfouse, C.Y. Wang, P.T. Huong, Advanced activation of persulfate by polymeric g-C$_3$N$_4$ based photocatalysts for environmental remediation: a review, J. Hazard. Mater. 413 (2021) 125324.

[22] R.B. Li, M.X. Cai, Z.J. Xie, Q.X. Zhang, Y.Q. Zeng, H.J. Liu, G.G. Liu, W.Y. Lv, Construction of heterostructured CuFe$_2$O$_4$/g-C$_3$N$_4$ nanocomposite as an efficient visible light photocatalyst with peroxydisulfate for the organic oxidation, Appl. Catal. B. 244 (2019) 974–982.

[23] Y. Deng, L. Li, H. Zeng, R. Tang, Z. Zhou, Y. Sun, C. Feng, D. Gong, J. Wang, Y. Huang, Unveiling the origin of high-efficiency charge transport effect of C$_3$N$_5$/C$_3$N$_4$ homojunction for activating peroxymonosulfate to degrade atrazine under visible light, Chem. Eng. J. 457 (2023) 141261.

[24] R. Tang, H. Zeng, D. Gong, Y. Deng, S. Xiong, L. Li, Z. Zhou, J. Wang, C. Feng, L. Tang, Thin-walled vesicular Triazole-CN-PDI with electronic n→π* excitation and directional movement for enhanced atrazine photodegradation, Chem. Eng. J. 451 (2023) 138445.

[25] C. Li, H. Wu, D. Zhu, T. Zhou, M. Yan, G. Chen, J. Sun, G. Dai, F. Ge, H. Dong, High-efficient charge separation driven directionally by pyridine rings grafted on carbon nitride edge for boosting photocatalytic hydrogen evolution, Appl. Catal. B. 297 (2021) 120433.

[26] Z.L. Weng, Y.F. Lin, B. Han, X.F. Zhang, Q. Guo, Y. Luo, X.W. Ou, Y. Zhou, J. Jiang, Donor-acceptor engineered g-C$_3$N$_4$ enabling peroxymonosulfate photocatalytic conversion to ^{1}O$_2$ with nearly 100% selectivity, J. Hazard. Mater. 448 (2023) 130869.

[27] Q. Li, L. Zhang, J. Liu, J. Zhou, Y. Jiao, X. Xiao, C. Zhao, Y. Zhou, S. Ye, B. Jiang, J. Liu, Porous carbon nitride thin strip: precise carbon doping regulating delocalized π-electron induces elevated photocatalytic hydrogen evolution, Small 17 (2021) e2006622.

[28] W. Ren, L. Xiong, X. Yuan, Z. Yu, H. Zhang, X. Duan, S. Wang, Activation of peroxydisulfate on carbon nanotubes: electron-transfer mechanism, Environ. Sci. Technol. 53 (2019) 14595–14603.

[29] Y. Nosaka, A.Y. Nosaka, Generation and detection of reactive oxygen species in photocatalysis, Chem. Rev. 117 (2017) 11302–11336.

[30] J. Wang, S. Wang, Effect of inorganic anions on the performance of advanced oxidation processes for degradation of organic contaminants, Chem. Eng. J. 411 (2021) 128392.

[31] W. Ren, C. Cheng, P. Shao, X. Luo, H. Zhang, S. Wang, X. Duan, Origins of electron-transfer regime in persulfate-based nonradical oxidation processes, Environ. Sci. Technol. 56 (2022) 78–97.

[32] R. Tang, D. Gong, Y. Deng, S. Xiong, J. Deng, L. Li, Z. Zhou, J. Zheng, L. Su, L. Yang, π-π Stacked step-scheme PDI/g-C$_3$N$_4$/TiO$_2$@Ti$_3$C$_2$ photocatalyst with enhanced visible photocatalytic degradation towards atrazine via peroxymonosulfate activation, Chem. Eng. J. 427 (2022) 131809.

[33] H. Che, C. Li, C. Li, C. Liu, H. Dong, X. Song, Benzoyl isothiocyanate as a precursor to design of ultrathin and high-crystalline g-C$_3$N$_4$-based donor–acceptor conjugated copolymers for superior photocatalytic H$_2$ production, Chem. Eng. J. 410 (2021).

[34] R. Tang, H. Zeng, C. Feng, S. Xiong, L. Li, Z. Zhou, D. Gong, L. Tang, Y. Deng, Twisty C-TiO$_2$/PCN S-scheme heterojunction with enhanced n→π* electronic excitation for promoted piezo-photocatalytic effect, Small (2023) e2207636.

[35] J. Oh, R.J. Yoo, S.Y. Kim, Y.J. Lee, D.W. Kim, S. Park, Oxidized carbon nitrides: water-dispersible, atomically thin carbon nitride-based nanodots and their performances as bioimaging probes, Chemistry 21 (2015) 6241–6246.

[36] Y. Shi, J. Li, D. Wan, J. Huang, Y. Liu, Peroxymonosulfate-enhanced photocatalysis by carbonyl-modified g-C$_3$N$_4$ for effective degradation of the tetracycline hydrochloride, Sci. Total. Environ. 749 (2020) 142313.

[37] Y. Deng, Z. Zhou, H. Zeng, R. Tang, L. Li, J. Wang, C. Feng, D. Gong, L. Tang, Y. Huang, Phosphorus and potassium co-doped g-C$_3$N$_4$ with multiple-locus synergies to degrade atrazine: insights into the depth analysis of the generation and role of singlet oxygen, Appl. Catal., B. 320 (2023) 121942.

[38] Y. Deng, L. Tang, G. Zeng, Z. Zhu, M. Yan, Y. Zhou, J. Wang, Y. Liu, J. Wang, Insight into highly efficient simultaneous photocatalytic removal of Cr(VI) and 2,4-diclorophenol under visible light irradiation by phosphorus doped porous ultrathin g-C$_3$N$_4$ nanosheets from aqueous media: performance and reaction mechanism, Appl. Catal., B. 203 (2017) 343–354.

[39] Z. Zeng, Y. Fan, X. Quan, H. Yu, S. Chen, S. Zhang, Energy-transfer-mediated oxygen activation in carbonyl functionalized carbon nitride nanosheets for high-efficient photocatalytic water disinfection and organic pollutants degradation, Water Res. 177 (2020) 115798.

[40] X. Duan, C. Su, J. Miao, Y. Zhong, Z. Shao, S. Wang, H. Sun, Insights into perovskite-catalyzed peroxymonosulfate activation: Maneuverable cobalt sites for promoted evolution of sulfate radicals, Appl. Catal. B. 220 (2018) 626–634.

[41] K.Z. Huang, H. Zhang, Direct electron-transfer-based peroxymonosulfate activation by iron-doped manganese oxide (δ-MnO$_2$) and the development of galvanic oxidation processes (GOPs), Environ. Sci. Technol. 53 (2019) 12610–12620.

[42] H. Ding, Y. Zhu, Y. Wu, J. Zhang, H. Deng, H. Zheng, Z. Liu, C. Zhao, In situ regeneration of phenol-saturated activated carbon fiber by an electro-peroxymonosulfate process, Environ. Sci. Technol. 54 (2020) 10944–10953.

[43] J.M. Dangwang Dikdim, Y. Gong, G.B. Noumi, J.M. Sieliechi, X. Zhao, N. Ma, M. Yang, J.B. Tchatchueng, Peroxymonosulfate improved photocatalytic degradation of atrazine by activated carbon/graphitic carbon nitride composite under visible light irradiation, Chemosphere 217 (2019) 833–842.

[44] Y. Zhou, J. Jiang, Y. Gao, J. Ma, S.Y. Pang, J. Li, X.T. Lu, L.P. Yuan, Activation of peroxymonosulfate by benzoquinone: a novel nonradical oxidation process, Environ. Sci. Technol. 49 (2015) 12941–12950.

[45] Z. Jiang, Y. Huang, Z. Zhu, S. Gao, Q. Lv, F. Li, Quenching singlet oxygen via intersystem crossing for a stable Li-O$_2$ battery, PNAS 119 (2022) e2202835119.

[46] Q. Wu, Y. Zhang, H. Liu, H. Liu, J. Tao, M.H. Cui, Z. Zheng, D. Wen, X. Zhan, Fe$_x$N produced in pharmaceutical sludge biochar by endogenous Fe and exogenous N doping to enhance peroxymonosulfate activation for levofloxacin degradation, Water Res. 224 (2022) 119022.

[47] A. Kumar, P. Singh, V.-H. Nguyen, Q. Van Le, T. Ahamad, S. Thakur, L. Huong Nguyen, P. Raizada, Rationally constructed synergy between dual-vacancies and Z-scheme heterostructured MoS$_{2−x}$/g-C$_3$N$_4$/Ca-α-Fe$_2$O$_3$ for high-performance photodegradation of sulfamethoxazole antibiotic from aqueous solution, Chem. Eng. J. 474 (2023) 145720.

[48] K. Sharma, V. Hasija, S. Patial, P. Singh, V.-H. Nguyen, A.K. Nadda, S. Thakur, P. Nguyen-Tri, C.C. Nguyen, S.Y. Kim, Q.V. Le, P. Raizada, Recent progress on MXenes and MOFs hybrids: structure, synthetic strategies and catalytic water splitting, Int. J. Hydrog. Energ. 48 (2023) 6560–6574.

[49] S. Xiong, H. Zeng, Y. Deng, C. Feng, R. Tang, Z. Zhou, L. Li, J. Wang, D. Gong, Insights into the dual Z-scheme and piezoelectricity co-driven photocatalyst for ultra-speed degradation of nitenpyram, Chem. Eng. J. 451 (2023) 138399.

[50] F. Xie, W. Zhu, P. Lin, J. Zhang, Z. Hao, J. Zhang, T. Huang, A bimetallic (Co/Fe) modified nickel foam (NF) anode as the peroxymonosulfate (PMS) activator: characteristics and mechanism, Sep. Purif. Technol. 296 (2022) 121429.

[51] X. Cheng, H. Guo, Y. Zhang, X. Wu, Y. Liu, Non-photochemical production of singlet oxygen via activation of persulfate by carbon nanotubes, Water Res. 113 (2017) 80–88.

[52] C. Sui, Z. Nie, H. Liu, G. Boczkaj, W. Liu, L. Kong, J. Zhan, Singlet oxygen-dominated peroxymonosulfate activation by layered crednerite for organic pollutants degradation in high salinity wastewater, J. Environ. Sci. 135 (2024) 86–96.

[53] J. Yu, L. Tang, Y. Pang, G. Zeng, H. Feng, J. Zou, J. Wang, C. Feng, X. Zhu, X. Ouyang, J. Tan, Hierarchical porous biochar from shrimp shell for persulfate activation: a two-electron transfer path and key impact factors, Appl. Catal., B. 260 (2020) 118160.

[54] R.S. Sprick, Z. Chen, A.J. Cowan, Y. Bai, C.M. Aitchison, Y.X. Fang, M. A. Zwijnenburg, A.I. Cooper, X.C. Wang, Water oxidation with cobalt-loaded linear conjugated polymer photocatalysts, Angew. Chem. Int. Ed. 59 (2020) 18695–18700.

[55] H. Wang, Y. Wu, T. Xiao, X.Z. Yuan, G.M. Zeng, W.G. Tu, S.Y. Wu, H.Y. Lee, Y. Z. Tan, J.W. Chew, Formation of quasi-core-shell In$_2$S$_3$/anatase TiO$_2$@metallic Ti$_3$C$_2$T$_x$ hybrids with favorable charge transfer channels for excellent visible-light-photocatalytic performance, Appl. Catal., B. 233 (2018) 213–225.

[56] H. Shi, Y. He, Y.B. Li, P.Y. Luo, Unraveling the synergy mechanism between photocatalysis and peroxymonosulfate activation on a Co/Fe bimetal-doped carbon nitride, Acs Catal. 13 (2023) 8973–8986.

[57] F. Chen, L.L. Liu, J.J. Chen, W.W. Li, Y.P. Chen, Y.J. Zhang, J.H. Wu, S.C. Mei, Q. Yang, H.Q. Yu, Efficient decontamination of organic pollutants under high salinity conditions by a nonradical peroxymonosulfate activation system, Water Res 191 (2021) 116799.

[58] R. Tang, D. Gong, Y. Deng, S. Xiong, J. Zheng, L. Li, Z. Zhou, L. Su, J. Zhao, π-π stacking derived from graphene-like biochar/g-C$_3$N$_4$ with tunable band structure for photocatalytic antibiotics degradation via peroxymonosulfate activation, J. Hazard. Mater. 423 (2022) 126944.

[59] Z.Y. Shen, H.Y. Zhou, Z.C. Pan, Y. Guo, Y. Yuan, G. Yao, B. Lai, Degradation of atrazine by Bi$_2$MoO$_6$ activated peroxymonosulfate under visible light irradiation, J. Hazard. Mater. 400 (2020) 123187.

[60] J.M.D. Dikdim, Y. Gong, G.B. Noumi, J.M. Sieliechi, X. Zhao, N. Ma, M. Yang, J. B. Tchatchueng, Peroxymonosulfate improved photocatalytic degradation of atrazine by activated carbon/graphitic carbon nitride composite under visible light irradiation, Chemosphere 217 (2019) 833–842.

[61] K.X. Wei, A. Armutlulu, Y.X. Wang, G. Yao, R.Z. Xie, B. Lai, Visible-light-driven removal of atrazine by durable hollow core-shell TiO$_2$@LaFeO$_3$ heterojunction coupling with peroxymonosulfate via enhanced electron-transfer, Appl. Catal.,. B 303 (2022) 120889.

[62] W.K. Jo, N.C.S. Selvam, Z-scheme CdS/g-C$_3$N$_4$ composites with RGO as an electron mediator for efficient photocatalytic H$_2$ production and pollutant degradation, Chem. Eng. J. 317 (2017) 913–924.

[63] T.S. Jamil, H.A. Abbas, R.A. Nasr, R.N. Vannier, Visible light activity of BaFe$_{1-x}$Cu$_x$O$_{3-\delta}$ as photocatalyst for atrazine degradation, Ecotox. Environ. Safe 163 (2018) 620–628.

[64] J. Guo, H. Sun, X. Yuan, L. Jiang, Z. Wu, H. Yu, N. Tang, M. Yu, M. Yan, J. Liang, Photocatalytic degradation of persistent organic pollutants by Co-Cl bond reinforced CoAl-LDH/Bi$_{12}$O$_{17}$Cl$_2$ photocatalyst: mechanism and application prospect evaluation, Water Res. 219 (2022) 118558.

[65] N. Li, R. Li, X. Duan, B. Yan, W. Liu, Z. Cheng, G. Chen, L. Hou, S. Wang, Correlation of active sites to generated reactive species and degradation routes of organics in peroxymonosulfate activation by co-loaded carbon, Environ. Sci. Technol. 55 (2021) 16163–16174.

[66] H. Zhang, C. Xie, L. Chen, J. Duan, F. Li, W. Liu, Different reaction mechanisms of·SO$_4^-$ and·OH with organic compound interpreted at molecular orbital level in Co (II)/peroxymonosulfate catalytic activation system, Water Res. 229 (2023) 119392.

[67] Y. Gao, Y. Zhou, S.Y. Pang, J. Jiang, Y.M. Shen, Y. Song, J.B. Duan, Q. Guo, Enhanced peroxymonosulfate activation via complexed Mn(II): a novel non-radical oxidation mechanism involving manganese intermediates, Water Res. 193 (2021) 116856.

[68] H. Zhang, X. Liu, J. Ma, C. Lin, C. Qi, X. Li, Z. Zhou, G. Fan, Activation of peroxymonosulfate using drinking water treatment residuals for the degradation of atrazine, J. Hazard. Mater. 344 (2018) 1220–1228.

[69] Y. Ji, C. Dong, D. Kong, J. Lu, New insights into atrazine degradation by cobalt catalyzed peroxymonosulfate oxidation: kinetics, reaction products and transformation mechanisms, J. Hazard. Mater. 285 (2015) 491–500.

[70] X. Sun, H. Qi, S. Mao, Z. Sun, Atrazine removal by peroxymonosulfate activated with magnetic CoFe alloy@N-doped graphitic carbon encapsulated in chitosan carbonized microspheres, Chem. Eng. J. 423 (2021) 130169.

[71] Y. Fan, Y. Ji, G. Zheng, J. Lu, D. Kong, X. Yin, Q. Zhou, Degradation of atrazine in heterogeneous Co$_3$O$_4$ activated peroxymonosulfate oxidation process: kinetics, mechanisms, and reaction pathways, Chem. Eng. J. 330 (2017) 831–839.

[72] G. Ye, P. Luo, Y. Zhao, G. Qiu, Y. Hu, S. Preis, C. Wei, Three-dimensional Co/Ni bimetallic organic frameworks for high-efficient catalytic ozonation of atrazine: mechanism, effect parameters, and degradation pathways analysis, Chemosphere 253 (2020) 126767.

[73] Y. An, X. Li, Z. Liu, Y. Li, Z. Zhou, X. Liu, Constant oxidation of atrazine in Fe(III)/ PDS system by enhancing Fe(III)/Fe(II) cycle with quinones: reaction mechanism, degradation pathway and DFT calculation, Chemosphere 317 (2023) 137883.

[74] W.J. Starnes, H.H. Hadley, Chlorophyll content of various strains of soybeans, glycine max (L.) merrill, Crop. Sci. 5 (1965) 9–11.